

FireFly-S: Exploiting Dual-Side Sparsity for Spiking Neural Networks Acceleration with Reconfigurable Spatial Architecture

Tenglong Li , Jindong Li , Guobin Shen , Dongcheng Zhao , Qian Zhang , Yi Zeng 

Abstract—Spiking Neural Networks (SNNs), with their brain-inspired structure using discrete spikes instead of continuous activations, are gaining attention for their potential of efficient processing on neuromorphic chips. While current SNN hardware accelerators often prioritize temporal spike sparsity, exploiting sparse synaptic weights offers significant untapped potential for even greater efficiency. To address this, we propose FireFly-S, a Sparse extension of the FireFly series. This co-optimized software-hardware design focusing on leveraging dual-side sparsity for acceleration. On the software side, we propose a novel algorithmic optimization framework that combines gradient rewiring for pruning and modified Learned Step Size Quantization (LSQ) tailored for SNNs, which achieves remarkable weight sparsity exceeding 85% and enables efficient 4-bit quantization with negligible accuracy loss. On the hardware side, we present an efficient dual-side sparsity detector employing a Bitmap-based sparse decoding logic to pinpoint the positions of non-zero weights and input spikes. The logic allows for the direct bypassing of redundant computations, thereby enhancing computational efficiency. Different from the overlay architecture adopted by previous FireFly series, we adopt a spatial architecture with inter-layer pipelining that can fully exploit the nature of Field-Programmable Gate Arrays (FPGAs). A spatial-temporal dataflow is also proposed to support such inter-layer pipelining and avoid long-term temporal dependencies. In experiments conducted on the MNIST, DVS-Gesture and CIFAR-10 datasets, the FireFly-S model achieves 85-95% sparsity with 4-bit quantization and the hardware accelerator effectively leverages the dual-side sparsity, delivering outstanding performance metrics of 10,047 FPS/W on MNIST, 3,683 FPS/W on DVS-Gesture, and 2,327 FPS/W on CIFAR-10.

Index Terms—Spiking neural networks, field-programmable gate array, hardware accelerator, dual-side sparsity, software-hardware co-design, inter-layer pipelining

Manuscript created 10 August 2024. This work was supported by the Chinese Academy of Sciences Foundation Frontier Scientific Research Program (ZDBS-LY- JSC013). (*Corresponding authors: Qian Zhang; Yi Zeng.*)

Tenglong Li, Jindong Li and Qian Zhang are with the School of Artificial Intelligence, University of Chinese Academy of Sciences, Beijing 100049, China, and also with the Brain-inspired Cognitive Intelligence Lab, Institute of Automation, Chinese Academy of Sciences, Beijing 100190, China (e-mail: litenglong2023@ia.ac.cn, lijindong2022@ia.ac.cn, q.zhang@ia.ac.cn).

Guobin Shen is with the School of Future Technology, University of Chinese Academy of Sciences, Beijing 100049, China, and also with the Brain-inspired Cognitive Intelligence Lab, Institute of Automation, Chinese Academy of Sciences, Beijing 100190, China (e-mail: shenguobin2021@ia.ac.cn).

Dongcheng Zhao is with the Brain-inspired Cognitive Intelligence Lab, Institute of Automation, Chinese Academy of Sciences, Beijing 100190, China (e-mail: zhaodongcheng2016@ia.ac.cn).

Yi Zeng is with the Brain-inspired Cognitive Intelligence Lab, Institute of Automation, Chinese Academy of Sciences, Beijing 100190, China, and University of Chinese Academy of Sciences, Beijing 100049, China, and Center for Excellence in Brain Science and Intelligence Technology, Chinese Academy of Sciences, Shanghai 200031, China (e-mail: yi.zeng@ia.ac.cn).

I. INTRODUCTION

AS a promising alternative to Artificial Neural Networks (ANNs), Spiking Neural Networks (SNNs) offer compelling advantages due to their high biological plausibility, effective event-driven processing, and inherent energy efficiency [1]. Moreover, spurred by both biological discoveries and advancements in deep learning, recent SNN algorithms have significantly closed the performance gap with ANNs [2]. However, real-world deployment of SNNs on hardware poses unique challenges stemming from their inherent complexity. In contrast to the dense, frame-based dataflow of ANNs, SNNs, characterized by spikes and time steps, exhibit a sparse and temporally correlated dataflow.

Despite the parallel processing capabilities of graphics processing units (GPUs), which are frequently used to deploy SNNs, their architecture is not tailored to the unique characteristics of SNNs. Specifically, GPUs lack consideration for event-driven processing and are not optimized for the 1-bit arithmetic operations commonly found in SNNs, highlighting the need for dedicated hardware solutions. In response to these shortcomings, researchers have explored the use of application-specific integrated circuits (ASICs) and field-programmable gate arrays (FPGAs). Notable developments include IBM's TrueNorth chip [3] and Intel's Loihi [4] and its successor Loihi2 [5], which are ASICs designed explicitly for SNNs and demonstrate marked improvements in energy efficiency and event-based processing. FPGAs also play a crucial role in SNNs acceleration, offering a flexible platform for exploring various optimization strategies. Some designs leverage this flexibility to enhance both arithmetic and memory efficiency, as in our previous work, FireFly [6] and FireFly v2 [7], while others focus on exploiting the sparse nature of spikes through event-driven processing [8] [9].

However, although these designs have made significant strides in improving the performance and energy efficiency of SNN hardware accelerators, they often overlook the potential for further optimization in areas such as network topology and synaptic connectivity. Exploiting the dual-side sparsity, specifically synaptic weight sparsity and activation spike sparsity, can substantially reduce both computational load and network parameters. Moreover, their reliance on high-precision data types like FP32, FP16 for weights and membrane potentials [9] [10], also increases the demand for DSP resources and large memory footprints, hindering deployment and limiting efficiency on resource-constrained platforms.

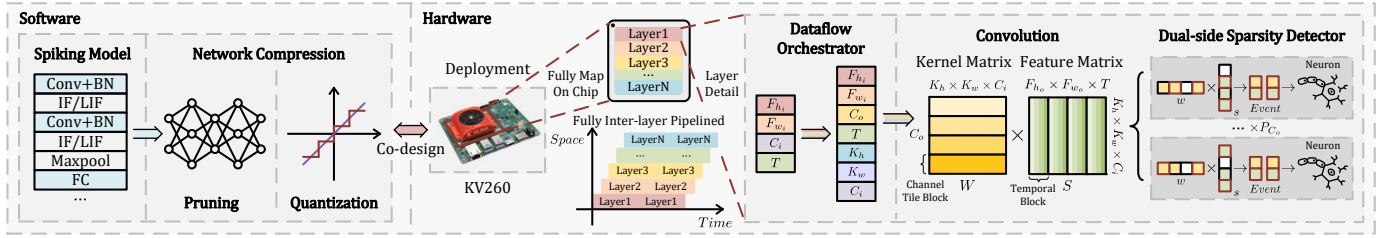


Fig. 1. Overview of the FireFly-S system architecture, combining the software optimization framework and hardware accelerator.

Based on these observations, we introduce FireFly-S, a co-optimized software-hardware design that capitalizes on dual-side sparsity for enhanced acceleration, as illustrated in Fig. 1. Our software stack initiates by pruning and quantizing the network weights during training, thereby inducing weight sparsity and low-bit representation to diminish both the model size and computational requirements. Subsequently, our hardware implementation maps the optimized SNN model onto FPGA fabric in a fully pipelined fashion. Each layer is equipped with a dedicated dataflow orchestrator that manages inter-layer data transfer, while parallel sparse detectors effectively leverage the dual-side sparsity of both sparse weights and spikes to optimize neuronal dynamics within each layer. Our contributions can be summarized as follows:

- 1) FireFly-S proposes an algorithmic optimization framework that combines gradient rewiring-based pruning and a Learned Step Size Quantization (LSQ) variant specifically tailored for SNNs, achieving over 85% weight sparsity with 4-bit quantization during training for various SNN models.
- 2) FireFly-S employs a Bitmap-based sparse decoding logic in the dual-side sparsity detector, enabling efficient exploitation of sparsity found in both activation spikes and synaptic weights. This approach directly skips all computations involving zero values, eliminating the inefficiency of performing unnecessary and idle calculations.
- 3) FireFly-S leverages a fully unfolded spatial architecture with inter-layer pipelining, eliminating off-chip memory access and concurrently processing multiple layers. We also presents a inter-layer dataflow tailored for SNNs, along with a dedicated logic to bridge the dataflow between layers, minimizing the need for extensive on-chip buffering.

The remaining sections of the paper are organized as follows: Section II reviews the background on SNNs compression and acceleration. Section III details the algorithmic optimization framework proposed in FireFly-S. Section IV describes the hardware acceleration strategy, encompassing both dataflow and sparse representation. Section V presents the hardware micro architecture of FireFly-S, featuring a sparse processor and dataflow orchestrator. Section VI provides experimental results and evaluations. Section VII concludes the paper and discusses future work.

II. BACKGROUND

A. Spiking Neuron Model and Dynamic Equation

Spiking Neural Networks utilize spiking neurons as their fundamental units, which communicate via binary spikes transmitted across weighted synapses. Although detailed models like the Izhikevich [11] and Hodgkin-Huxley [12] neurons accurately capture biological neuron behavior, the computationally less demanding Integrate-and-Fire (IF) [13] and Leaky Integrate-and-Fire (LIF) [14] models are more commonly employed in current SNN implementations [9] [15].

The LIF neuron model simulates the passive decay of the membrane potential towards a resting state due to ion leakage, as well as the generation of a spike when the integrated input current drives the membrane potential above a certain threshold. This behavior is mathematically described by the following differential equation:

$$\tau_m \frac{dV}{dt} = -V + R_m I(t) \quad (1)$$

where V is the membrane potential, R_m is the membrane resistance, τ_m is the membrane time constant, and $I(t)$ is the input current. When the membrane potential reaches a threshold V_{th} , the neuron emits a spike and resets its potential to a resting value V_{reset} . As a discrete event-driven model, the LIF neuron can be described by the following equation:

$$I_i(t) = \sum_j w_{ij} s_j(t) + b_i \quad (2)$$

$$V_i(t) = V_i(t-1) + \frac{1}{\tau_m} (R_m I_i(t) - V_i(t-1)) \quad (3)$$

$$V_i(t) = \begin{cases} V_{reset}, & \text{if } V_i(t) > V_{th} \\ V_i(t), & \text{otherwise} \end{cases} \quad (4)$$

Equation (2) accumulates the input current $I_i(t)$ from all presynaptic neurons j with weights w_{ij} and spikes $s_j(t)$, as well as a bias term b_i . Equation (3) updates the membrane potential $V_i(t)$ based on the input current and the membrane time constant. As for IF neurons, this decay process is absent, and the membrane potential simply integrates the input current without any leakage. Equation (4) checks if the membrane potential exceeds the threshold V_{th} , emits a spike if true and resets the potential to V_{reset} . In practical implementations, the membrane time constant τ_m is often set to 2, and the potential resetting value V_{reset} is set to 0, with the membrane resistance R_m normalized to 1.

These spiking neuron models bring two key distinctions from traditional ANNs. First, the temporal dimension T in SNNs involves the processing of membrane potentials over time, introducing temporal dependencies. Second, since neurons only fire spikes when their membrane potential exceeds a threshold, the neuron activity can be sparse [16] [17]. This binary and sparse nature of spike events presents both challenges and opportunities for efficient hardware implementation.

B. Spiking Neural Networks Compression

As previously mentioned, SNNs are inherently sparse and event-driven, making them well-suited for efficient processing on neuromorphic chips. However, deploying SNNs on hardware platforms presents challenges due to their temporal dynamics and the memory requirements for storing membrane potentials. To overcome these challenges, researchers have explored various compression techniques, such as weight pruning and quantization, to further reduce parameter size and computational complexity in SNNs.

Accordingly, Compressing SNNs through sparsity regularization and ADMM optimization was proposed by Deng *et al.* [18]. Chen *et al.* [19] introduced a gradient-based rewiring method, jointly optimizing weight values and connections for pruning. Putra *et al.* [20] developed the Q-SpiNN framework, which quantizes SNNs by exploring various quantization schemes and precision levels, guided by a reward function. Wei *et al.* [21] propose a Weight-Spike Dual Regulation method to mitigate the performance degradation caused by quantization.

However, while pruning can induce dual-side sparsity in both weights and activations, and quantization can further boost the compression ratio, there is limited work on effectively combining these two techniques during training, especially in a hardware-friendly manner that considers the efficiency constraints presented by neuromorphic hardware for SNNs, such as fully integer arithmetic within neuron computations.

C. Spiking Neural Networks Accelerators

Hardware accelerators for SNNs can be broadly categorized into two approaches: general-purpose optimization and specialized acceleration. General-purpose methods focus on optimizing hardware architecture or modules for broader applicability. In contrast, specialized accelerators exploit the unique characteristics of SNNs, such as sparsity and event-driven dynamics, to achieve higher efficiency. For instance, Li *et al.* presented FireFly [6] and FireFly-v2 [7], which leverage the DSP48E2 units in Xilinx FPGAs and a spatial-temporal dataflow to optimize the accelerator for overlay architectures. Targeting event-driven characteristics, Panchapakesan *et al.* proposed SyncNN [8], which encodes only activated neurons and quantizes LeNet to 4 bits. Chen *et al.* introduced SiBrain [10], featuring a sparse detection and response unit based on a channel-cache and blockmultiplex design.

Despite these advancements, current architectures often fail to utilize sparsity effectively, focusing primarily on spike sparsity and neglecting dual-side sparsity. Furthermore, many designs rely on overlay architectures that necessitate off-chip

memory access, which can be inefficient. Notably, networks are typically quantized to 8 to 16 bits [6] [7] [10], leading to increased storage demands. In contrast, SyncNN's 4-bit quantization supports only a lightweight LeNet model [8], highlighting limitations in scalability. There remains a significant gap in research on fully on-chip spatial architectures that could enhance throughput and power efficiency by facilitating entire inference processes on-chip. This underscores the urgent need for software-hardware co-design methodologies that can exploit both dual-side sparsity and the potential of low-bit quantization in SNNs, thereby enabling more efficient computation and reduced memory footprints.

III. ALGORITHMIC OPTIMIZATION

As discussed earlier, while SNNs offer inherent spike sparsity, they also pose challenges in terms of computational complexity and memory footprints. This section first discusses compression sequence, focusing on the order of pruning and quantization. We then introduce how FireFly-S implements pruning and quantization during training, where pruning enables hardware exploitation through dual-side sparsity and quantization further enhances the efficiency of computation and memory.

A. Compression Sequence

The sequence of pruning and quantization significantly influence the final performance of SNNs. Quantization is typically performed before pruning to preserve the network's accuracy, as quantization ensures more paths for optimization before the connectivity is reduced by pruning. However, pruning can also affect the distribution of weights, potentially making the quantization scale and zero-point inappropriate for the pruned network. This can lead to suboptimal performance or require recalibration of the quantization parameters to maintain accuracy.

Another strategy is to perform pruning and quantization simultaneously, jointly optimizing the weight values and connections. This approach can explore a larger search space and potentially find better solutions, especially when pruning and quantization are integrated into the training process, which also avoids the need for additional post-training compression steps, retraining, or fine-tuning. This is precisely the strategy employed by FireFly-S, as shown in the Fig. 2 enabling it to achieve a favorable balance between compression and accuracy.

B. Compression Methodologies

The pruning algorithm we adopt is based on gradient rewiring [19]. In this method, each synaptic weight w is represented as $w = s \odot \text{ReLU}(\theta)$, where θ represents the synaptic parameter, and \odot denotes the element-wise product. The sign factor s , determined by the sign of the initial weight, indicates whether the connection is excitatory or inhibitory. This representation is illustrated in the left part of Fig. 2. During pruning, the optimization focuses on driving some θ values towards non-positive values, effectively eliminating

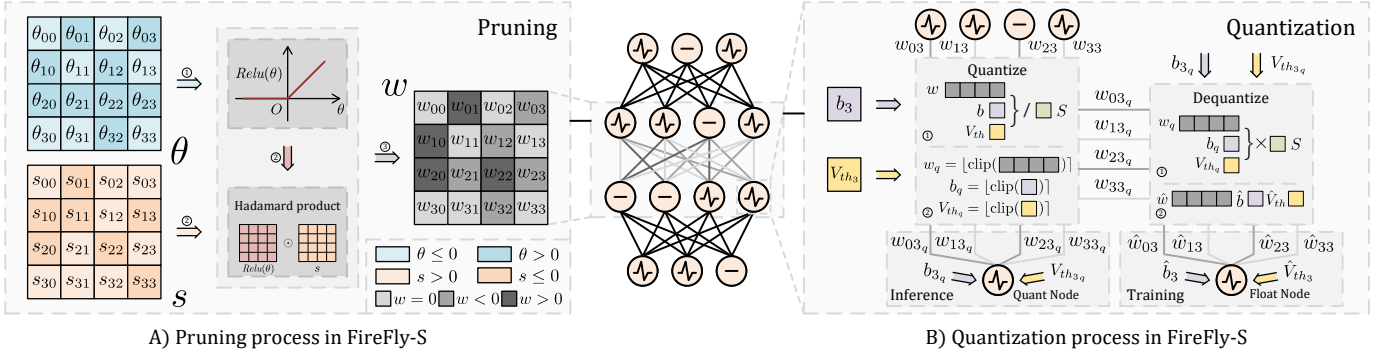


Fig. 2. Compression process in FireFly-S. A) Pruning process. B) Quantization process, including both inference and training stages.

the corresponding connections. Our approach extends this method by incorporating weight decay λ , which penalizes the magnitude of θ during optimization, driving more weights towards zero. Besides, to enable more comprehensive network compression, we apply this pruning strategy to both convolutional and fully connected layers, including bias parameters that optimized by AdamW [22].

Due to the adoption of fine-grained pruning, there is a likelihood that some weights within an output channel dimension might be entirely zero. In ANNs, even if the weights are zero, the presence of a bias can still result in a non-zero output for a layer. Thus, the kernel of that output channel cannot be pruned solely based on weight values. However, SNNs exhibit different behavior due to the presence of a neuron threshold. In SNNs, even the accumulated bias across the temporal dimension might not exceed the threshold, particularly when the neuron model includes leaky currents. Consequently, if the neuron remains inactive (silent) throughout, it indicates that the kernel of that output channel could potentially be pruned. Algorithm 1 provided simulates the inference process to identify such silent output channels and prunes them accordingly.

For quantization, we adopt the principles of Learned Step Size Quantization (LSQ) [23]. To enable gradient-based optimization of the quantization scale, LSQ employs the straight-through estimator (STE) [24], which approximates the gradient of the otherwise non-differentiable quantization operation. The quantization process is defined as:

$$r_q = Q(r, S, Q_N, Q_P) \quad (5)$$

$$= \lfloor \text{clip}(r/S, -Q_N, Q_P) \rfloor \quad (6)$$

$$\hat{r} = r_q \times S \quad (7)$$

Here, r represents the real-valued input, S the quantization scale, r_q the quantized value, and \hat{r} the dequantized value. The function $Q(\cdot)$ denotes the quantization operation and $\lfloor \cdot \rfloor$ denotes rounding to the nearest integer. Q_N and Q_P define of the minimum and maximum quantized absolute values, respectively, ensuring the clipped value remains within the designated range. The gradient of the quantization error with respect to the scale S is:

$$\frac{\partial \hat{r}}{\partial S} = \begin{cases} -r/S + \lfloor r/S \rfloor & \text{if } -Q_N < r/S < Q_P \\ -Q_N & \text{if } r/S \leq -Q_N \\ Q_P & \text{if } r/S \geq Q_P \end{cases} \quad (8)$$

Algorithm 1: Temporal Membrane Potential Evaluation for Channel Pruning

Input:

- Number of output channels C_o
- Number of time steps T
- Array of thresholds \mathbf{V}_{th} (one threshold per channel)
- Array of biases \mathbf{b} (one bias per channel)

Output: List of active channels A

- 1 Initialize membrane potentials matrix V of size $C_o \times T$ to zero;
 - 2 Initialize list of active channels $A \leftarrow []$;
 - 3 **for** $c_o \leftarrow 0$ to $C_o - 1$ **do**
 - 4 **for** $t \leftarrow 0$ to $T - 1$ **do**
 - 5 $V[c_o][t] \leftarrow V[c_o][t - 1] + \mathbf{b}[c_o]$;
 - 6 **if** $V[c_o][t] > \mathbf{V}_{th}[c_o]$ **then**
 - 7 $A \leftarrow A \cup \{c_o\}$;
 - 8 **break**;
 - 9 **end**
 - 10 **end**
 - 11 **end**
 - 12 **return** A ;
-

While LSQ has proven effective for quantizing ANNs, it is not directly applicable to SNNs and is not optimized for fully integer computation. This is because the bias of layers and the threshold of spiking neurons are still real-valued, and using the same quantization scale optimized for weights on the bias and threshold can lead to accuracy degradation.

Motivated by the success of STE in approximating gradients for quantization, we present the LSQ variant specifically designed for SNNs. Unlike traditional LSQ, our approach jointly optimizes the quantization scale across weights, biases, and neuronal thresholds during training. We employ a shared scale for weights within the same channel, as well as for the corresponding bias and neuronal threshold. Additionally, we allow a wider quantization range for biases and thresholds and enable gradient descent on the neuronal thresholds. This facilitates end-to-end learning of quantized SNNs, as illustrated by the inference and training processes of a single layer depicted in the right part of Fig. 2. During training, weights, biases, and threshold values undergo quantization and dequantization, with

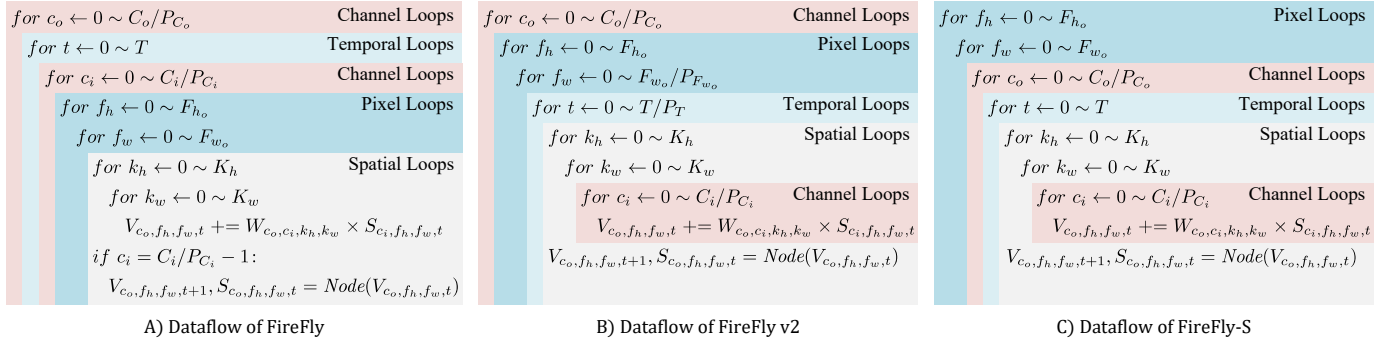


Fig. 3. Comparison of the dataflow in FireFly-S to its previous version FireFly and FireFly v2. A) FireFly’s dataflow design. B) FireFly v2’s dataflow design. C) FireFly-S’s dataflow design.

the dequantized parameters used for forward and backward propagation. Conversely, inference relies solely on quantized parameters for forward propagation, eliminating the need for dequantization, scale storage, and associated computations.

By jointly optimizing quantization and incorporating pruning, while explicitly considering the unique characteristics of SNNs, this approach enables high compression rate and fully integer computation deployment for more efficient inference. Section VI provides a detailed analysis of accuracy and compression outcomes across various networks, benchmarked against E3NE [25] and SyncNN [8].

IV. HARDWARE ACCELERATION STRATEGY

To unlock the full potential of inter-layer pipelining in hardware acceleration, a carefully chosen parallelism scheme and a consistent dataflow pattern are essential. Besides, efficiently exploiting the dual-side sparsity of SNNs hinges on a suitable sparse representation that minimizes memory footprint while maximizing throughput. This section delves into the specific dataflow and parallelism strategies employed by FireFly-S, followed by an analysis of the chosen sparse representation and its impact on hardware acceleration efficiency.

A. Dataflow and Parallelism Schemes

FireFly v2 demonstrated the importance of carefully designed dataflow in SNN implementations, focusing on an overlay architecture to balance spatial and temporal dimensions. FireFly-S, however, takes a different route by embracing a spatial architecture, an approach whose dataflow considerations remain unexplored for SNNs on FPGAs. The challenge lies in fully harnessing the potential of spatial architectures, which offer complete network pipelining but demand meticulously designed dataflow to ensure consistent and efficient data movement between input and output.

Fig. 3 illustrates the dataflow evolution within the FireFly series. Here, C_o , C_i , F_{h_o} , F_{w_o} , K_h , K_w , and T represent the number of output channels, input channels, output feature map height, output feature map width, kernel height, kernel width, and temporal dimension, respectively. V , W , and S denote membrane voltage, synaptic weight, and activation spike. Parallelism levels are denoted by P , with P_{C_o} , P_{C_i} , $P_{F_{w_o}}$, and P_T corresponding to parallelism across output

channels, input channels, output feature map width, and the temporal dimension.

FireFly’s initial design, with its outer-loop temporal processing, suffers from inefficiencies compared to the spatial-temporal approach of FireFly v2. This is because handling the temporal dimension in the outer loop necessitates storing membrane voltage values for extended periods, resulting in a significant memory footprint proportional to $P_{C_o} \times F_{h_o} \times F_{w_o}$. FireFly v2 mitigates this by processing the temporal dimension in a more inner loop, effectively minimizing the impact of long-term temporal dependencies. This optimization reduces the required memory storage for membrane voltage to $P_{C_o} \times P_{F_{w_o}}$, a value determined by the level of parallelism.

However, a key distinction arises between FireFly-S and its predecessors. While both FireFly and FireFly v2 utilize overlay architectures, relying on off-chip memory for feature map and weight storage, FireFly-S adopts a spatial architecture to enable full inter-layer pipelining. This shift necessitates a departure from FireFly v2’s dataflow strategy. In detail, solutions are required to address the two main challenges posed by spatial architectures: 1) the tight on-chip memory constraints, which demand efficient memory utilization, and 2) the need for a consistent dataflow pattern to ensure efficient processing across layers and avoid pipeline stalls.

Directly applying FireFly v2’s dataflow to a spatial architecture would prove inefficient. FireFly v2, designed with off-chip memory reliance, employs an output-channel outermost loop. This approach, while functional, leads to excessive on-chip memory consumption in a spatial architecture. Computing each output channel requires access to all input feature maps, necessitating storage of all layer feature maps on-chip, amounting to $L \times F_{h_o} \times F_{w_o} \times T \times C_i$ memory, where L represents the number of layers. Such demands would deteriorate the limits of on-chip memory.

Besides, the output channel in this layer is the input channel in the next layer, so it is challenging to design a consistent dataflow pattern. But we can minimize the storage and data movement. Employing an output-channel outermost loop and an input-channel innermost loop, as in FireFly v2, would lead to significant pipeline stalls in a spatial architecture. Each layer would need to wait for all output channel computations of the previous layer to complete, so it could not match the need of non-stall pipeline for spatial architecture.

TABLE I
MEMORY STORAGE COMPARISON OF FIREFLY-S
WITH PREVIOUS VERSIONS

	V_{buf}	S_{buf}
FireFly	$P_{C_o} \times F_{h_o} \times F_{w_o}$	$F_{h_o} \times F_{w_o} \times T \times C_i$
FireFly v2	$P_{C_o} \times P_{F_{w_o}}$	$F_{h_o} \times F_{w_o} \times T \times C_i$
FireFly-S	P_{C_o}	$((K_h - 1) \times F_{w_o} + K_w) \times T \times C_i$

To address these challenges, we have restructured the dataflow by placing the channel loops inside the pixel loops while maintaining the temporal loop nested within the output channel loops. This configuration provides two main benefits. Firstly, by confining the temporal loop, it allows the membrane voltage to accumulate consecutively, removing the need to store values for each time step. Secondly, by embedding the channel loop within the pixel loop, it eliminates long-term dependencies between channels, thereby minimizing data movement and ensuring a consistent dataflow. This optimization retains only the essential feature map data necessary for network operations and data reuse, effectively reducing the required feature map storage by a factor of $F_{h_o} / (K_h - 1)$. Table I presents the results of this optimization, detailing the membrane voltage and feature map storage requirements, denoted by V_{buf} and S_{buf} respectively.

B. Sparse Representation Analysis

While pruning and the inherent spike sparsity in SNNs yield high dual-side sparsity, the choice of sparse representation significantly impacts the memory footprint and computational efficiency of hardware accelerators. Several sparse representation schemes exist, including Coordinate Lists (COO), Compressed Sparse Row (CSR), and Bitmap representations.

Coordinate Lists (COO) offer a simple and intuitive representation, storing non-zero values alongside their corresponding indices. Compressed Sparse Row (CSR) improves upon this by compressing row indices, storing row offsets instead of explicit indices. While requiring additional decoding logic to locate non-zero values, CSR reduces memory footprint by eliminating redundant row index storage. Bitmap representation takes a different approach, storing non-zero values with a corresponding mask indicating their presence. This method implicitly encodes addresses within the mask, eliminating the need for explicit indices.

This difference in encoding strategies leads to a key trade-off: While COO and CSR formats offer the advantage of storing only the indices of non-zero values, these indices can require a larger number of bits compared to the single bit used in Bitmap representation. Bitmap, on the other hand, utilizes a bit array to represent the presence or absence of all values, regardless of whether they are zero or non-zero. This difference in storage strategy means that the sparsity of the matrix plays a crucial role in determining which format is more memory-efficient.

Furthermore, decoding non-zero pairs in a dual-side sparse matrix using COO and CSR necessitates separate decoding for weights and spikes. This separate decoding can lead to

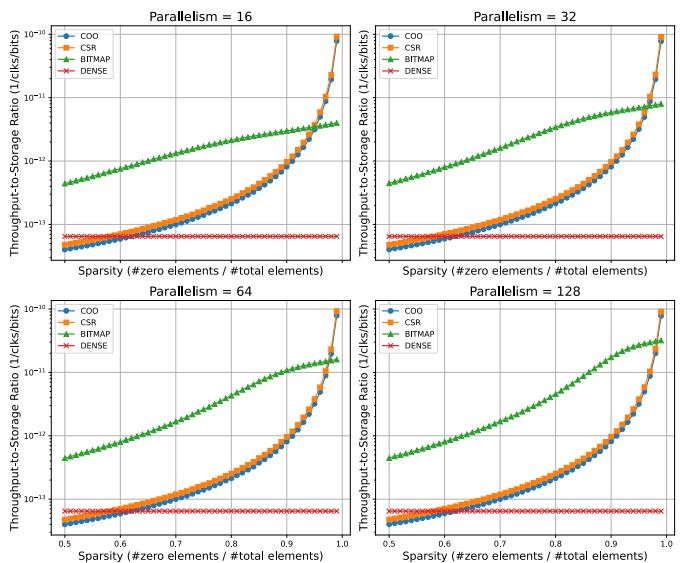


Fig. 4. Throughput-to-storage ratio versus sparsity for COO, CSR, and Bitmap sparse representations and dense representation. Data points are plotted at 0.01 sparsity intervals.

pipeline stalls when mismatches occur, ultimately reducing overall throughput. Bitmap representation, however, allows for simultaneous decoding and direct identification of matching non-zero pairs, mitigating these performance bottlenecks.

Therefore, considering the critical importance of both memory storage and throughput in hardware design, we conduct an experimental analysis to evaluate these trade-offs. Throughput is measured as the number of non-zero pairs processed per cycle, while storage is determined by calculating the number of bits required to store the sparse matrix in each format. Both CSR and COO decoding logic are assumed to decode one non-zero value per cycle for both weight and spike decoders concurrently, and Bitmap decoding logic is assumed to decode one non-zero pair per cycle for each vector pair with a length of 16/32/64/128, which indicates the parallelism for a layer in our hardware architecture. Notably, the Bitmap logic still consumes one clock cycle when there is no non-zero pair for the current vector pair.

This analysis, conducted within a specific experimental environment, simulating a convolutional operation with parameters $(T, C_o, C_i, F_{h_o}, F_{w_o}, K_h, K_w) = (4, 64, 32, 16, 16, 3, 3)$. The setup represents a single layer within the 9-layer network for CIFAR-10 recognition discussed in Section VI, and the selection doesn't affect the overall trend observed. Fig. 4 illustrates the throughput-to-storage ratio across various sparsity levels, comparing the performance of COO, CSR, and Bitmap sparse representations against a dense representation. While COO and CSR outperform Bitmap at extremely high sparsity levels (above 95%) due to Bitmap's larger memory footprint, Bitmap consistently demonstrates superior performance at other sparsity levels. This advantage is further amplified with larger vector pair lengths, extending its applicability to a wider range of sparsity. Notably, in Figure 4, the sparsity level is shared by both synaptic weights and activation spikes. Experiments indicate that the sparsity of activation spikes ranges

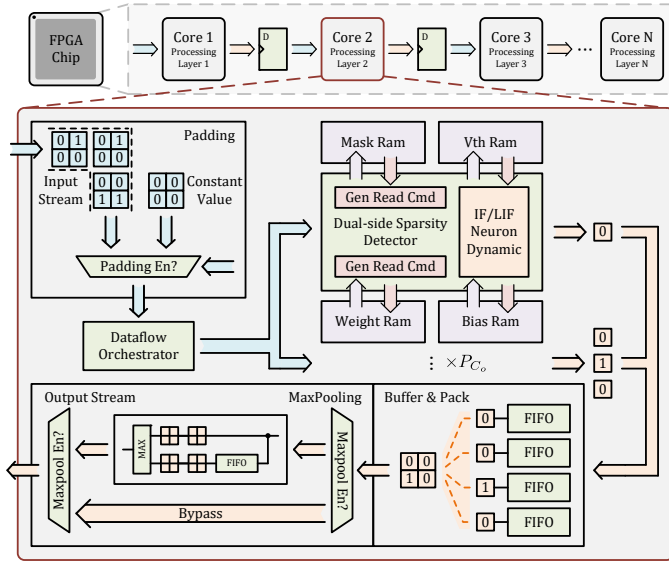


Fig. 5. Inter-layer Pipelined Architecture of FireFly-S. Each pipeline stage performs one layer inference and includes modules for Padding, Dataflow Orchestration, Dual-side Sparsity Detection, and Maxpooling.

from 70% to 90%. Therefore, the sparsity of the weights must be significantly higher to reach the threshold where Bitmap becomes less efficient than COO or CSR. Given these observations, we adopt the Bitmap representation in FireFly-S, prioritizing its greater generality and higher throughput-to-storage ratio across a wide range of sparsity levels.

V. HARDWARE MICRO ARCHITECTURE

The hardware microarchitecture of the FireFly-S is intricately designed to harness the dual-side sparsity characteristic of SNNs. It features a spatial layout that incorporates inter-layer pipelining, as illustrated in Fig. 5. Each pipeline stage is tailored to process a single layer of inference, equipped with specific modules including Padding, Dataflow Orchestrator, Dual-side Sparsity Detector, and Maxpooling.

The Padding module dynamically adjusts input dimensions for convolutional layers, adding padding in "same" mode to match output and input sizes, while bypassing padding for "valid" mode or fully connected layers. The Dataflow Orchestrator is pivotal in ensuring consistent dataflow between layers to maintain pipeline efficiency. It also efficiently manages the im2col operation for SNNs, essential for reorganizing input data into a format suitable for convolution operations, all while maintaining a membrane potential storage-free approach. The Dual-side Sparsity Detector module optimizes computations by identifying matching nonzero elements in both activation spikes and synaptic weights, enabling computational savings by bypassing unnecessary operations. Then, it generates specific read commands for relevant data (weights, biases, masks, thresholds) and efficiently updates neuron dynamics in the IF/LIF neuron model. Finally, the optional Maxpooling module provides spatial downsampling of the output, the output stream is then pipelined and fed into the next core or layer for further processing.

This section provides an in-depth exploration of the key elements of FireFly-S, particularly the Dataflow Orchestrator and the Dual-side Sparsity Detector, detailing their essential roles and functionalities within the broader system architecture.

A. Dataflow Orchestrator

As discussed in Section IV, spatial architectures require a consistent dataflow pattern. However, achieving this consistency presents a challenge due to the conflicting dataflow requirements between the output of one layer and the input of the next. Specifically, the membrane potential storage-free calculation in FireFly-S necessitates placing the output channel loop **outside** the temporal loop. This arrangement contrasts with the input dataflow of the subsequent layer, which requires the channel loop to be **inside** the temporal loop for efficient processing. Furthermore, convolution operations introduce an additional complexity: the need for the im2col operation to transform the input feature map into a matrix format suitable for convolution.

To reconcile these conflicting dataflow requirements and manage the im2col operation, FireFly-S employs a dedicated Dataflow Orchestrator, as illustrated in Fig. 6. This FIFO-based logic utilizes on-chip RAM divided into two sectors. The first sector functions as a minimal line buffer specifically for the im2col operation, storing only the data necessary to maintain the convolution window as the input feature map streams in. The size of this sector is determined by the input dimension and kernel size. Crucially, data within this sector is reused multiple times, as dictated by the parallelism level and data dimensions, to ensure continuous operation when parallelism cannot fully unroll the convolution. The remaining on-chip RAM serves as a configurable holding area, acting as a buffer for incoming spike feature maps from upstream processing. This holding area prevents pipeline stalls that would otherwise occur when the reused sector is full. Additionally, it provides a transition buffer for switching convolution windows. For clarity, the example in Fig. 6 depicts a parallelism level of 1, with an input dataflow of $(F_{h_i}, F_{w_i}, C_i, T)$ being transformed to the output dataflow of $(F_{h_i}, F_{w_i}, C_o, T, K_h, K_w, C_i)$.

The orchestrator leverages a combination of status registers, implemented as simple counters, and some stride counters. The status registers, chained to form loop iterators, pinpoint the current position within the dataflow. These registers don't directly determine memory addresses but provide signals that guide the stride counters in generating the correct addresses for fetching data from the RAM. The use of stride counters for base address and offset address, each with its own specific increment value, allows the orchestrator to navigate the non-sequential memory access patterns required by the implicit im2col and data transpositions, eliminating the need for computationally expensive multiplication operations.

The orchestrator manages data access through a push pointer and a pop pointer, mirroring the functionality of a traditional FIFO buffer. While the push pointer logic mirrors that of a standard FIFO, the pop pointer is determined by the combined values of the base and offset counters. The base counter marks the starting position of the current convolution window within

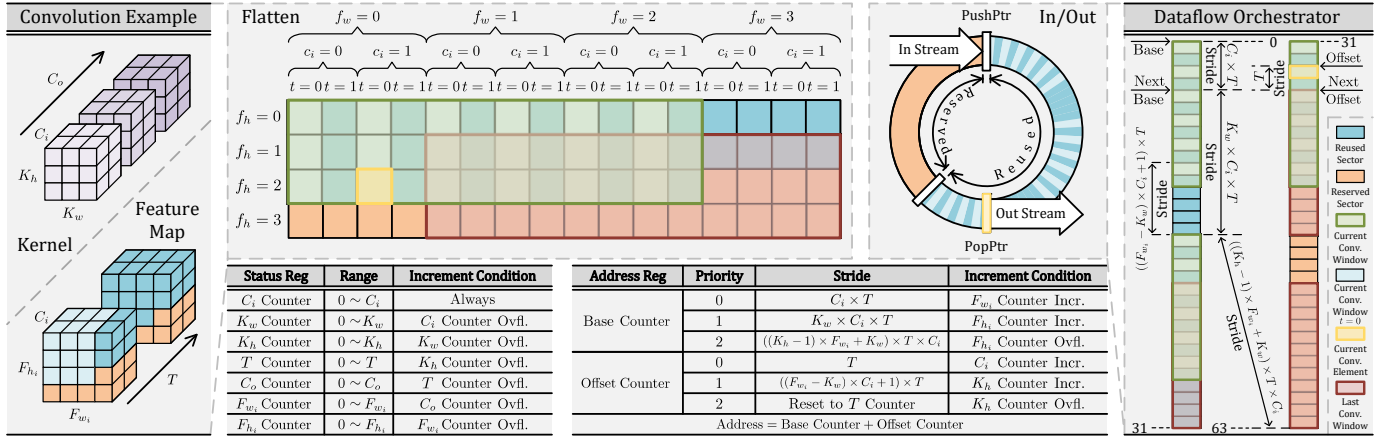


Fig. 6. Dataflow Orchestrator in FireFly-S, illustrated with an example where $(T, C_o, C_i, F_{w_i}, F_{h_i}, K_{w_i}, K_{h_i}) = (2, 2, 3, 4, 4, 3, 3)$ and $(P_{C_o}, P_{C_i}) = (1, 1)$. The "Priority" column in the table indicates the order in which stride is taken, with higher numbers representing higher priority.

the RAM, while the offset counter traverses elements within that window.

For "valid" convolution with stride 1, the base counter increment for the dataflow coordinator adapts based on the window's position within the feature map. Under normal operation, the increment is simply $C_i \times T$, reflecting the number of data elements in the previous window's channel and temporal dimensions. In addition to this regular increment, specific adjustments are needed for efficient transitions between rows and feature maps. After processing the last window of a row, the base counter must jump to the beginning of the next row, requiring an increment of $(K_w \times C_i \times T)$ to bypass the remaining $(K_w - 1)$ columns of the previous row. Similarly, transitioning to a new feature map necessitates an increment of $((K_h - 1) \times F_{w_i} + K_w) \times C_i \times T$ to address the start of the new feature map's data. This ability to directly address and access data within the RAM, regardless of its position, contributes to the efficiency of Dataflow Orchestrator. Traditional line buffers, reliant on sequential shifting, would inevitably incur overhead during both row and feature map transitions, as they must sequentially shift data to align the buffer with the required starting position for processing.

The offset counter works in conjunction with the base counter to pinpoint the exact data address within each convolution window. To prioritize the channel loop over the temporal loop for efficient processing, the offset counter typically increments by T , reordering the data stream from the input's temporal-within-channel organization to a channel-within-temporal organization. When transitioning between rows within the convolution window, the offset counter's stride changes to $((F_{w_i} - K_w) \times C_i + 1) \times T$ to account for the memory layout shift between rows. Furthermore, during membrane potential storage-free calculations, the offset counter dynamically adapts when switching iterators in the temporal dimension. It resets to the value stored in the temporal counter within the status register and then continues incrementing using the previously described stride patterns.

Besides its role in managing the dataflow, the design logic of Dataflow Orchestrator also leverages the regularity of data access patterns, which are dictated by consistent stride pat-

terns, to pre-calculate base and offset counter values. This pre-calculation enables pipelined address generation for the FIFO's pop pointer, efficiently determining the next data element for processing and significantly enhancing throughput. Furthermore, the predictability arising from these consistent strides allows the FIFO's full and empty signals to be implemented as registers. This design choice minimizes combinational logic delays, improving timing closure and ultimately contributing to support the 333MHz working frequency across our entire architecture in our experiment, as discussed in Section VI.

B. Dual-side Sparsity Detector

After passing through the Dataflow Orchestrator, the activation spikes are buffered and aligned with their corresponding weight mask data, which is represented in Bitmap format. This prepared data is then processed by the Dual-side Sparsity Detector, as illustrated in Fig. 7.

The lower left corner of the Fig. 7 illustrates the initial transformation of the original sparse weight matrix into a Bitmap format. This process involves evaluating each matrix element to ascertain its non-zero status, resulting in the creation of a bitmap mask alongside a separate collection of non-zero values. These bitmaps are then segmented into vectors, each sized according to the input channel parallelism, P_{C_i} . A higher P_{C_i} allows for larger bitmap segments, amplifying the throughput-to-storage advantage inherent in Bitmap representation.

Following segmentation, both the bitmaps and non-zero values are distributed across the output channel parallelism, P_{C_o} . Consequently, each detector within the Dual-side Sparsity Detector is assigned a segment of the non-zero weight RAM along with its corresponding bitmap mask RAM, where the length of each bitmap segment corresponds to P_{C_i} . This arrangement ensures that each detector operates with a precise portion of data, exploiting the fact that computations for each output channel are independent and can be performed in parallel. A higher P_{C_o} allows for more detectors to operate in parallel, further enhancing throughput. This higher P_{C_o} , representing the number of parallel output elements calculated in this layer, directly translates to a potentially higher P_{C_i} in

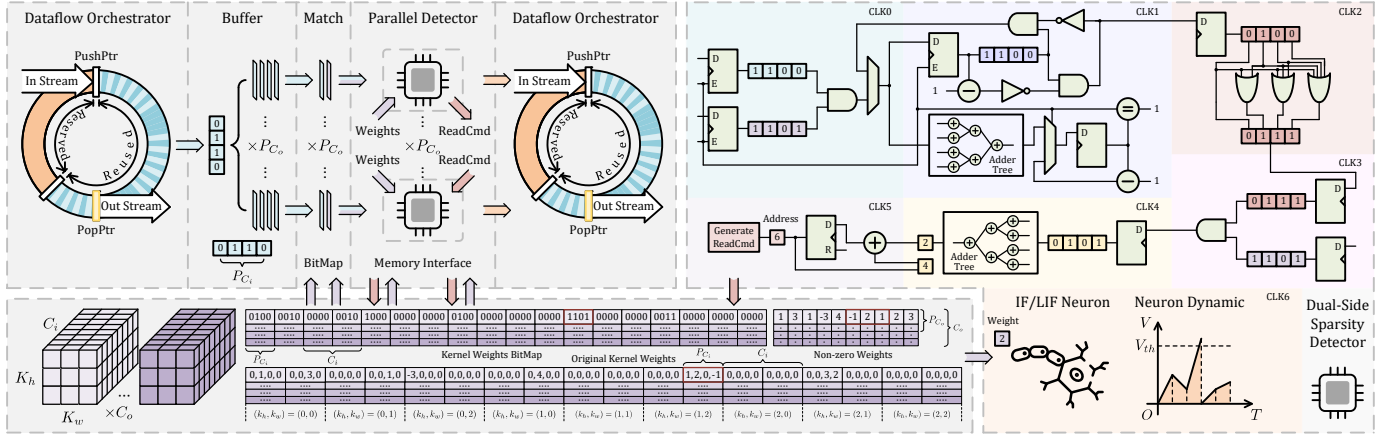


Fig. 7. Schematic of the Dual-side Sparsity Detector in FireFly-S, illustrated with configuration parameters $(C_o, C_i, K_{w_i}, K_{h_i}) = (4, 8, 3, 3)$ and parallelism parameters $(P_{C_o}, P_{C_i}) = (2, 4)$.

the next layer. This is because these parallel output elements are then assembled into a complete output vector, which in turn, forms the input spikes vector for the subsequent layer, as shown in the upper left corner of Fig. 7.

The processing flow within each detector, as depicted in the upper right corner of Fig. 7, begins with the reception of input spikes alongside a corresponding weight mask. At CLK0, a bitwise AND operation is executed between the vector pair, yielding a result denoted as x , which identifies active events. Following this, at CLK1, an adder tree efficiently tallies the number of non-zero pairs in x , and this count is stored in a decrement counter. The counter serves a dual purpose: it indicates the completion of processing non-zero pairs and signals the readiness to receive a new input vector pair.

In this stage, a one-hot encoded output, y , is generated through the logical expression $y = x \wedge \neg(x-1)$. This operation positions a '1' at the index of the first non-zero pair in x . The register holding x is then updated using the expression $x = x \wedge \neg y$, which ensures that processed pairs are not reactivated in subsequent cycles. This process repeats until all non-zero pairs in x are processed, producing a series of one-hot encoded output vectors y that accurately represent the activation pattern for the current input.

The next stage utilizes the one-hot vector y to generate a new vector with bits set from the least significant bit up to the index where '1' is set in y . For example, if y is 4'b0100, which indicates the third position, the generated vector would be 4'b0111. This vector is then subjected to a bitwise AND operation with the weight mask to pinpoint active indices that align with the mask. Continuing with the example, if the weight mask is 4'b1101, the result of the AND operation between 4'b0111 and 4'b1101 would be 4'b0101. This result, obtained at CLK3, allows the detector at the following cycle (CLK4) to determine the precise storage offset — 2 in this example — of the weight data corresponding to the '1' in the original one-hot vector 4'b0100 using an adder tree. At CLK5, the calculated offset is accumulated into an offset register. This accumulated offset is then added to the base address stored in a base address register to generate the final address for accessing the weight data, thus preparing the read

command for the specific weight data. Finally, at CLK6, the weight data is fetched from the RAM and used to perform IF/LIF neuron model computation. It is important to note that the membrane potential is stored in a register, and due to the dedicated dataflow, the voltage for each time step is temporally stored in the register and reused for the next time step.

For clarity, Fig. 7 does not explicitly illustrate the interactions with bias and threshold RAMs as depicted in Fig. 5. However, these interactions are straightforward: each output channel's neuron dynamics require the addition of bias, and the membrane potential must be compared with the threshold to decide if a spike should be generated. Since both bias and threshold are assigned per channel (reflecting per-channel quantization), and because the bias is always added and the threshold is always checked against the membrane potential to determine spike generation, the reading addresses for both are represented by an incrementing counter.

Moreover, to improve efficiency during the dual-side sparse acceleration process involving weight and spike vectors, a specific optimization is employed. Typically, if the bitwise AND operation between the spike vectors and the weight vector bitmap results in all zeros, it would lead to a wasted cycle due to the absence of valid nonzero pairs. To counter this inefficiency, we incorporate the bias, treated as a constant input of '1' with a corresponding weight equal to the bias value, which is processed in each time step. By designing logic to absorb the cycle that would have been wasted on detection into the cycle used for adding the bias, we ensure that the bias effectively replaces the ineffective cycle. This eliminates unnecessary idle clock cycles and enhances the efficiency of the Dual-side Sparsity Detector.

Fig. 8 depicts the optimized logic employed in the weight and bias retrieval process. This process utilizes handshake logic with *valid* and *ready* signals; however, since the bias is always considered valid, its corresponding *valid* signal is disregarded. Central to this mechanism is the *biasCycleReg*, a register determining the need to utilize bias addition to mitigate idle cycles. Specifically, when the weight retrieval logic's *isBubble* signal is low and the *last* signal is high—indicating an impending time step increment—the *biasCycleReg* is set

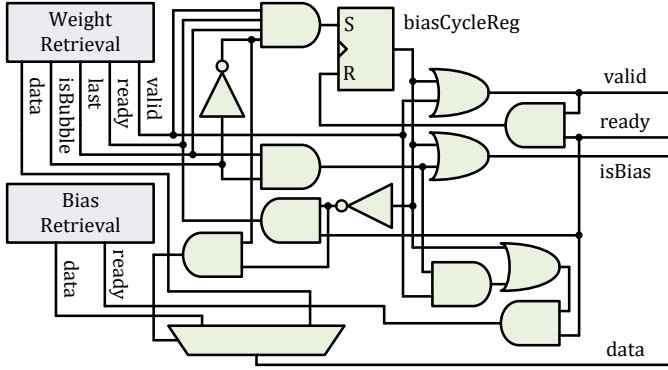


Fig. 8. Optimized logic for weight and bias retrieval in the Dual-side Sparsity Detector, illustrating the strategic implementation of bias addition to mitigate idle detector cycles.

TABLE II
CONFIGURATION OF SNN MODELS

Model	Configuration
SCNN5	1x28x28-8c3p1-16c3p2-mp2-32c3p1-mp2-64c3p1-64c3p1-mp2-10fc
SCNN7	2x48x48-16c3p1-32c3p1-mp2-32c3p1-64c3p1-mp2-64c3p1-128c3p1-mp2-128c3p1-10
SCNN9	3x32x32-16c3p1-32c3p1-mp2-32c3p1-64c3p1-mp2-64c3p1-128c3p1-mp2-128c3p1-256c3p1-mp2-10

high, signaling that the current data pertains to weight (*isBias* is low), and thus, the bias will be added in the subsequent cycle. Conversely, if *isBubble* is high and *last* is also high, the *biasCycleReg* resets, allowing for the immediate addition of the bias within the current cycle to optimize efficiency by eliminating idle cycles.

VI. IMPLEMENTATION AND EXPERIMENTS

A. Experiments Setup

To evaluate the performance of FireFly-S, we conduct a series of experiments using various SNN models, specifically SCNN5, SCNN7, and SCNN9 models with 5, 7, and 9 convolutional layers. Detailed configurations of these models are presented in Table II, where 'c3p1' indicates a 3x3 convolution kernel with padding of 1, 'mp2' represents max pooling with a 2x2 filter and stride of 2, and '10fc' represents a fully connected layer with 10 output neurons. These models are trained on the MNIST, DVS-Gesture, and CIFAR-10 datasets, respectively. For testing, all models are deployed on the Xilinx Zynq Ultrascale+ FPGA, utilizing the KV260 Vision AI Starter Kit, which is specifically designed for the deployment of edge-based applications.

On the software side, FireFly-S leverages the Brain-Inspired Cognitive Engine (BrainCog) [26] and represents a substantial progression in the software-hardware co-design endeavors within the BrainCog project [27]. The SNN models used in this project are trained using the comprehensive infrastructure provided by BrainCog, ensuring robust and efficient performance metrics that enhance the system's overall functionality.

On the hardware side, FireFly-S is developed using SpinalHDL, and the corresponding Verilog code is produced by the

TABLE III
PARALLELISM LEVELS FOR SCNN5, SCNN7, SCNN9 MODELS

Model	Parallelism P_{C_o}
SCNN5	(14, 25, 20, 14, 5)
SCNN7	(19, 23, 32, 16, 32, 19, 1)
SCNN9	(32, 16, 21, 13, 26, 13, 20, 10, 1)

TABLE IV
RESOURCE USAGE OF FIREFLY-S ON XILINX ULTRASCALE KV260

Model	LUTs	FFs	CARRY8s	BRAMs
SCNN5	30911(26%)	55986(24%)	268(2%)	5(3%)
SCNN7	55234(47%)	98731(42%)	473(3%)	11(8%)
SCNN9	84641(72%)	139780(60%)	1545(11%)	76.5(53%)

TABLE V
DETAILED RESOURCE USAGE BY MODULE
IN THE SIXTH CONVOLUTION LAYER OF SCNN9 ON FIREFLY-S

Module	LUTs	FFs	CARRY8s	BRAMs
Padding Module	35	20	0	0
Dataflow Orchestrator	243	258	13	0.5
Dual-side Sparsity Detector	296	507	9	6
Maxpooling Module	387	612	0	0

SpinalHDL compiler. These Verilog files are then synthesized and implemented via Xilinx Vivado 2023.2, and the power consumption estimates are derived from the reports generated by the Vivado Design Suite.

B. Parallelism Setup

As outlined in Section V, FireFly-S leverages parallelism to enhance throughput and computational efficiency. Determining the optimal parallelism levels for the inter-layer pipelined architecture is crucial to maximizing performance within device constraints. This optimization is achieved through a two-step process.

The first step focuses on balancing the workload across all pipeline stages. This balance is essential to ensure uniform processing times, preventing bottlenecks that could hinder overall performance. We quantify the workload of each stage using the number of multiplex-accumulate (MAC) operations, factoring in the sparsity of computations. The MAC count, representing the total number of algebraic operations required for a convolution layer, is estimated as follows:

$$\text{MAC} \propto C_o \times C_i \times F_{w_o} \times F_{h_o} \times K_w \times K_h \times T \quad (9)$$

Sparsity significantly impacts the actual computational load. We assess sparsity in two stages. First, we calculate the spike sparsity (s_1) by inferring several batches of random images. Second, we determine the weight sparsity (s_2). The overall sparsity affecting the workload is the product of these two factors. Given that each stage in our pipeline has P_{C_o} parallel units, the estimated workload for each unit becomes:

$$\text{Workload per Unit} = \text{MAC} \times \frac{s_1 \times s_2}{P_{C_o}}. \quad (10)$$

TABLE VI
COMPARISON WITH RELATED WORK FOR MULTIPLE IMAGE CLASSIFICATION TASKS USING SNNs FOR MULTIPLE DATASET.

Work	Network	Dataset	Acc.	Prec.	FPS	Power	FPS/W	Freq.	Device	
Minitaur [28]	784-500-500-10	MNIST	92.00	16	108	1.500	72.00	75	xc6slx150t	
Han <i>et al.</i> [29]	784-1024-1024-10	MNIST	97.06	16	161	0.477	337.53	200	xc7z045	
Zhang <i>et al.</i> [30]	784-512-384-10	MNIST	98.00	8	909	0.700	1298.57	-	xc7vx690t	
Ju <i>et al.</i> [31]	28x28-64c5-p2-64c5-p2-128-10	MNIST	98.94	8	164	4.600	35.65	150	xczu9eg	
Fang <i>et al.</i> [32]	28x28-32c3-p2-32c3-p2-256-10	MNIST	99.20	16	133	4.500	29.55	125	xczu9eg	
Ye <i>et al.</i> [33]	32x32-32c3-p2-32c3-p2-256-10	MNIST	99.10	16	820	0.982	835.03	200	xc7k325t	
		FMNIST	90.29		833		848.27			
		SVHN	82.15		826		841.14			
E3NE [25]	LeNet5	MNIST	99.30	3	3400	3.400	1000.00	200	xcvu13p	
	AlexNet	CIFAR10	80.60	6	14.3	4.700	3.04	150		
	VGG11	CIFAR100	65.00		6.1	5.000	1.22			
SyncNN [8]	LeNet-L	MNIST	99.60	4	1629	0.400 ¹	4072.50	200	xczu9eg	
	NIN	CIFAR10	88.09	8	147		367.5			
	VGG13	SVHN	95.65		65		162.50			
FireFly [6]	28x28-16c3-64c3-p2-128c3-p2-256c3-256c3-10	MNIST	98.12	8	2036	3.100	656.78	300	xczu3eg	
	32x32-16c3-64c3-p2-128c3-128c3-p2-256c3-256c3-p2-512c3-10	CIFAR10			91.36		4975			1015.31
FireFly v2 [7]	48x48-16c3-64c3-64c3-p2-128c3-128c3-p2-256c3-256c3-p2-512c3-512c3-10	DVS-Gesture	89.29	8	2342	4.900	477.95	500 ²	xczu5ev	
					282		90.97			
Ours	SCNN5	MNIST	98.03	4	10047	1.301	7722.52	333	xczu5ev	
	SCNN7	DVS-Gesture	92.05		3683		1.821			2022.52
	SCNN9	CIFAR10	87.00		2327		3.799			612.53

¹ SyncNN calculates power usage by measuring the active power consumption of the FPGA board (24.5 W) and subtracting the static power measured when the board is idle (24.1 W). Conversely, it is believed that most existing research acquires power metrics directly from the Vivado report.

² The base clock frequency of FireFly v2 is 250 MHz, with a DSP double data rate clock of 500 MHz.

By adjusting the parallelism levels, we ensure an even workload distribution across all pipeline stages. In the second step, we gradually increase the parallelism levels until one of two conditions is met: either the available hardware resources, such as Look-Up Tables (LUTs) or RAM, become the limiting factor, or the system achieves the desired performance speed. This iterative adjustment of the parallelism configuration ensures that the pipeline stages are optimized for maximum throughput and efficiency within the given resource constraints. Table III presents the setup of parallelism levels for the SCNN5, SCNN7, SCNN9 models in our experiments.

C. Resource and Performance Evaluation

FireFly-S demonstrates its versatility by efficiently training and deploying various SNN models tailored to distinct image classification tasks. This evaluation includes three advanced SNN architectures—SCNN5, SCNN7, and SCNN9—tested across three diverse datasets. These datasets encompass both traditional static images and dynamic, neuromorphic data streams, each presenting unique classification challenges.

Table IV details the resource utilization of FireFly-S across various model deployments on the Xilinx Ultrascale KV260, equipped with an xczu5ev chip. As model sizes increase, we observe a corresponding rise in the utilization of the resources, this trend is attributable to an increase in the number of layers and the characteristic of spatial architectures. Notably, the efficient 4-bit quantization and the intrinsic spike-based operation of the SNNs allow inference processes to operate

without any DSP Slices, relying solely on LUTs. Additionally, the application of model size compression through 4-bit quantization and high sparsity levels significantly reduces BRAM usage. For example, despite the 8-bit quantized weight parameters of SCNN9 still requiring 9.5Mb—surpassing the chip’s BRAM capacity of 5.1Mb and 3.5Mb of Distributed RAM—the reduction techniques lower the BRAM demand to just 53%. This enhanced efficiency supports the feasible deployment of larger models on the chip.

Table V offers a detailed breakdown of resource usage by each module within a single layer of FireFly-S, indicating that the Dataflow Orchestrator and Dual-side Sparsity Detector are the primary consumers of resources when the Maxpooling module is inactive. Note that the reported resource usage for the Dual-side Sparsity Detector, except for BRAMs, is calculated by dividing by the parallelism level (26 in this experiment) Therefore, while increasing parallelism in FireFly-S can enhance performance, it will also raise the consumption of LUTs and FFs, potentially reaching the resource limits.

In terms of performance, the evaluation uses the Frames Per Second per Watt (FPS/W) metric to assess energy efficiency, recognizing the challenge in comparing studies with varying benchmark complexities. FPS/W comparisons are particularly informative when the models being compared have similar classification accuracies, ensuring a fair assessment of both energy efficiency and algorithmic optimization at a given performance level.

Table VI demonstrates that FireFly-S adeptly adjusts to a va-

riety of datasets and models, delivering accuracies on par with those documented in other studies while operating at increased frequencies due to its fully pipelined inter-layer architecture. Additionally, FireFly-S showcases notable energy efficiency. When compared with E3NE, it achieves $\times 7.7$ higher FPS/W on MNIST, $\times 202$ higher FPS/W on CIFAR10, and a significant 6.4% improvement in accuracy. Against SyncNN, FireFly-S attains $\times 1.9$ higher FPS/W on MNIST and $\times 1.7$ higher FPS/W on CIFAR10, despite SyncNN only accounting for dynamic power. These enhancements are supported by two critical advancements: algorithmic improvements that allow for the deployment of large, compressed models on resource-limited FPGAs without sacrificing accuracy, and the incorporation of parallel Dual-side Sparsity Detectors in each layer to exploit network sparsity and boost throughput.

Furthermore, Table VI highlights prevalent data precisions in SNN implementations, specifically 16-bit and 8-bit. While the study by Gerlinghoff et al. [25] applies 3-bit quantization to LeNet5, it utilizes 6-bit precision for more complex models like AlexNet and VGG11 to maintain acceptable accuracy levels. In a similar vein, Panchapakesan et al. [8] implement percentile-based quantization in SyncNN, achieving 4-bit precision for LeNet-L and 8-bit for NiN and VGG13. However, attempts to apply 4-bit quantization to NiN and VGG13 resulted in significant accuracy reductions of 7.86% and 8.96%, respectively. In contrast, the FireFly-S model maintains high accuracy not only with 4-bit quantization across various models but also achieves notable sparsity levels of 93.82% in SCNN5, 93.26% in SCNN7, and 86.12% in SCNN9. Additionally, our hardware architecture uniquely supports dual-side sparsity exploitation, distinguishing it from previous implementations.

Finally, it is important to highlight that although our chosen device, the xczu5ev, is an edge device, FireFly-S still demonstrates significant improvements across all benchmarks. By utilizing a larger device such as the xczu7ev in the ZCU104, the inference performance can be further enhanced due to the substantially greater number of LUT resources available, which alleviates the bottlenecks experienced with the xczu5ev and supports higher levels of parallelism. Additionally, it is noteworthy that our model is fully mapped on-chip, which means that each layer utilizes fewer resources compared to an overlay architecture. Despite this, our design achieves remarkable performance without any off-chip memory access, thereby eliminating external power consumption typically associated with overlay architectures.

VII. CONCLUSIONS

In this work, we introduce a high-energy-efficient and reconfigurable hardware accelerator for SNNs, leveraging a software-hardware co-design approach to optimize energy efficiency during SNN inference. On the software side, our approach includes a quantization-aware and pruning-aware training method, which enables the training of SNN models at 4-bit quantization and 85-95% sparsity with minimal accuracy loss. This training strategy not only allows the deployment of large SNN models on-chip but also enhances calculation logic

utilization by introducing weight sparsity through pruning. On the hardware side, we capitalize on the natural sparsity of spikes inherent to SNNs and the engineered sparsity of weights to accelerate processing. This is effectively exploited by our Dual-side Sparsity Detector, which accelerates processing by leveraging both types of sparsity and skipping the unnecessary calculations. Additionally, our architecture is designed to be fully pipelined, enhancing throughput. The Dataflow Orchestrator plays a critical role in maintaining consistent dataflow between layers, minimizing stalls, and simplifying logic to reduce resource consumption. We validate the reconfigurability of our FireFly-S accelerator by evaluating various deep SNN models across multiple datasets. Utilizing commercially available FPGA edge devices offers a more practical and feasible solution compared to other existing hardware platforms. Future work will focus on enhancing the SNN hardware infrastructure further, aiming for ultra-high compression rates and addressing the decline in efficiency that occurs when sparsity levels are excessively high in Bitmap representation.

REFERENCES

- [1] W. Maass, "Networks of spiking neurons: the third generation of neural network models," *Neural networks*, vol. 10, no. 9, pp. 1659–1671, 1997.
- [2] G. Shen, D. Zhao, and Y. Zeng, "Backpropagation with biologically plausible spatiotemporal adjustment for training deep spiking neural networks," *Patterns*, vol. 3, no. 6, 2022.
- [3] F. Akopyan, J. Sawada, A. Cassidy, R. Alvarez-Icaza, J. Arthur, P. Merolla, N. Imam, Y. Nakamura, P. Datta, G.-J. Nam et al., "Truenorth: Design and tool flow of a 65 mw 1 million neuron programmable neurosynaptic chip," *IEEE transactions on computer-aided design of integrated circuits and systems*, vol. 34, no. 10, pp. 1537–1557, 2015.
- [4] M. Davies, N. Srinivasa, T.-H. Lin, G. Chinya, Y. Cao, S. H. Choday, G. Dimou, P. Joshi, N. Imam, S. Jain et al., "Loihi: A neuromorphic manycore processor with on-chip learning," *Ieee Micro*, vol. 38, no. 1, pp. 82–99, 2018.
- [5] G. Orchard, E. P. Frady, D. B. D. Rubin, S. Sanborn, S. B. Shrestha, F. T. Sommer, and M. Davies, "Efficient neuromorphic signal processing with loihi 2," in *2021 IEEE Workshop on Signal Processing Systems (SiPS)*. IEEE, 2021, pp. 254–259.
- [6] J. Li, G. Shen, D. Zhao, Q. Zhang, and Y. Zeng, "Firefly: a high-throughput hardware accelerator for spiking neural networks with efficient dsp and memory optimization," *IEEE Transactions on Very Large Scale Integration (VLSI) Systems*, 2023.
- [7] J. Li, G. Shen, D. Zhao, Q. Zhang, and Y. Zeng, "Firefly v2: Advancing hardware support for high-performance spiking neural network with a spatiotemporal fpga accelerator," *IEEE Transactions on Computer-Aided Design of Integrated Circuits and Systems*, 2024.
- [8] S. Panchapakesan, Z. Fang, and J. Li, "Syncnn: Evaluating and accelerating spiking neural networks on fpgas," *ACM Transactions on Reconfigurable Technology and Systems*, vol. 15, no. 4, pp. 1–27, 2022.
- [9] Y. Liu, Y. Chen, W. Ye, and Y. Gui, "Fpga-nhap: A general fpga-based neuromorphic hardware acceleration platform with high speed and low power," *IEEE Transactions on Circuits and Systems I: Regular Papers*, vol. 69, no. 6, pp. 2553–2566, 2022.
- [10] Y. Chen, W. Ye, Y. Liu, and H. Zhou, "Sibrain: A sparse spatio-temporal parallel neuromorphic architecture for accelerating spiking convolution neural networks with low latency," *IEEE Transactions on Circuits and Systems I: Regular Papers*, 2024.
- [11] E. M. Izhikevich, "Which model to use for cortical spiking neurons?" *IEEE transactions on neural networks*, vol. 15, no. 5, pp. 1063–1070, 2004.
- [12] A. L. Hodgkin and A. F. Huxley, "A quantitative description of membrane current and its application to conduction and excitation in nerve," *The Journal of physiology*, vol. 117, no. 4, p. 500, 1952.
- [13] L. F. Abbott, "Lapicque's introduction of the integrate-and-fire model neuron (1907)," *Brain research bulletin*, vol. 50, no. 5-6, pp. 303–304, 1999.
- [14] P. Dayan and L. F. Abbott, *Theoretical neuroscience: computational and mathematical modeling of neural systems*. MIT press, 2005.

- [15] Q. Chen, C. Gao, and Y. Fu, "Cerebron: A reconfigurable architecture for spatiotemporal sparse spiking neural networks," *IEEE Transactions on Very Large Scale Integration (VLSI) Systems*, vol. 30, no. 10, pp. 1425–1437, 2022.
- [16] R. Yin, Y. Kim, Y. Li, A. Moitra, N. Satpute, A. Hambitzer, and P. Panda, "Workload-balanced pruning for sparse spiking neural networks," *IEEE Transactions on Emerging Topics in Computational Intelligence*, 2024.
- [17] R. Yin, Y. Li, A. Moitra, and P. Panda, "Mint: Multiplier-less integer quantization for energy efficient spiking neural networks," in *2024 29th Asia and South Pacific Design Automation Conference (ASP-DAC)*. IEEE, 2024, pp. 830–835.
- [18] L. Deng, Y. Wu, Y. Hu, L. Liang, G. Li, X. Hu, Y. Ding, P. Li, and Y. Xie, "Comprehensive snn compression using admm optimization and activity regularization," *IEEE transactions on neural networks and learning systems*, vol. 34, no. 6, pp. 2791–2805, 2021.
- [19] Y. Chen, Z. Yu, W. Fang, T. Huang, and Y. Tian, "Pruning of deep spiking neural networks through gradient rewiring," *arXiv preprint arXiv:2105.04916*, 2021.
- [20] R. V. W. Putra and M. Shafique, "Q-spinn: A framework for quantizing spiking neural networks," in *2021 International Joint Conference on Neural Networks (IJCNN)*. IEEE, 2021, pp. 1–8.
- [21] W. Wei, Y. Liang, A. Belatreche, Y. Xiao, H. Cao, Z. Ren, G. Wang, M. Zhang, and Y. Yang, "Q-snns: Quantized spiking neural networks," *arXiv preprint arXiv:2406.13672*, 2024.
- [22] I. Loshchilov and F. Hutter, "Decoupled weight decay regularization," *arXiv preprint arXiv:1711.05101*, 2017.
- [23] S. K. Esser, J. L. McKinstry, D. Bablani, R. Appuswamy, and D. S. Modha, "Learned step size quantization," *arXiv preprint arXiv:1902.08153*, 2019.
- [24] Y. Bengio, N. Léonard, and A. Courville, "Estimating or propagating gradients through stochastic neurons for conditional computation," *arXiv preprint arXiv:1308.3432*, 2013.
- [25] D. Gerlinghoff, Z. Wang, X. Gu, R. S. M. Goh, and T. Luo, "E3ne: An end-to-end framework for accelerating spiking neural networks with emerging neural encoding on fpgas," *IEEE Transactions on Parallel and Distributed Systems*, vol. 33, no. 11, pp. 3207–3219, 2021.
- [26] Y. Zeng, D. Zhao, F. Zhao, G. Shen, Y. Dong, E. Lu, Q. Zhang, Y. Sun, Q. Liang, Y. Zhao *et al.*, "Braincog: A spiking neural network based, brain-inspired cognitive intelligence engine for brain-inspired ai and brain simulation," *Patterns*, vol. 4, no. 8, 2023.
- [27] "Braincog: Brain-inspired cognitive intelligence engine." [Online]. Available: <http://www.brain-cog.network>.
- [28] D. Neil and S.-C. Liu, "Minitaur, an event-driven fpga-based spiking neural network accelerator," *IEEE transactions on very large scale integration (VLSI) systems*, vol. 22, no. 12, pp. 2621–2628, 2014.
- [29] J. Han, Z. Li, W. Zheng, and Y. Zhang, "Hardware implementation of spiking neural networks on fpga," *Tsinghua Science and Technology*, vol. 25, no. 4, pp. 479–486, 2020.
- [30] J. Zhang, H. Wu, J. Wei, S. Wei, and H. Chen, "An asynchronous reconfigurable snn accelerator with event-driven time step update," in *2019 IEEE Asian Solid-State Circuits Conference (A-SSCC)*. IEEE, 2019, pp. 213–216.
- [31] X. Ju, B. Fang, R. Yan, X. Xu, and H. Tang, "An fpga implementation of deep spiking neural networks for low-power and fast classification," *Neural computation*, vol. 32, no. 1, pp. 182–204, 2020.
- [32] H. Fang, Z. Mei, A. Shrestha, Z. Zhao, Y. Li, and Q. Qiu, "Encoding, model, and architecture: Systematic optimization for spiking neural network in fpgas," in *Proceedings of the 39th International Conference on Computer-Aided Design*, 2020, pp. 1–9.
- [33] W. Ye, Y. Chen, and Y. Liu, "The implementation and optimization of neuromorphic hardware for supporting spiking neural networks with mlp and cnn topologies," *IEEE Transactions on Computer-Aided Design of Integrated Circuits and Systems*, vol. 42, no. 2, pp. 448–461, 2022.